J. Fluid Mech. (2008), *vol.* 615, *pp.* 371–399.
doi:10.1017/S0022112008003716 Printed in the United Kingdom

Turbulent flow between counter-rotating concentric cylinders: a direct numerical simulation study

S. DONG

Center for Computational and Applied Mathematics, Department of Mathematics, Purdue University, West Lafayette, IN 47907, USA

(Received 12 March 2008 and in revised form 21 July 2008)

We report three-dimensional direct numerical simulations of the turbulent flow between counter-rotating concentric cylinders with a radius ratio 0.5. The inner- and outer-cylinder Reynolds numbers have the same magnitude, which ranges from 500 to 4000 in the simulations. We show that with the increase of Reynolds number, the prevailing structures in the flow are azimuthal vortices with scales much smaller than the cylinder gap. At high Reynolds numbers, while the instantaneous small-scale vortices permeate the entire domain, the large-scale Taylor vortex motions manifested by the time-averaged field do not penetrate a layer of fluid near the outer cylinder. Comparisons between the standard Taylor–Couette system (rotating inner cylinder, fixed outer cylinder) and the counter-rotating system demonstrate the profound effects of the Coriolis force on the mean flow and other statistical quantities. The dynamical and statistical features of the flow have been investigated in detail.

1. Introduction

Taylor–Couette systems with differentially rotating cylinders can accommodate a surprisingly large variety of flow states, both laminar and turbulent, as well as states with the co-existence of laminar and turbulent regions (Andereck, Liu & Swinney 1986). The transition diagrams established by early workers (Coles 1965; Andereck *et al.* 1986; Litschke & Roesner 1998) which map out different regimes of the flow have proved to be indispensable guides to the experimental and theoretical explorations that followed of physical mechanisms responsible for the transitions (Van Atta 1966; Hegseth *et al.* 1989; Colovas & Andereck 1997; Goharzadeh & Mutabazi 2001; Prigent *et al.* 2002).

The present study concerns the situation of counter-rotating cylinders, that is, with the inner and the outer cylinders rotating in opposite directions. The flow geometry is characterized by the radius ratio, $\eta = R_i/R_o$, where R_i and R_o are, respectively, the radii of the inner and outer cylinders, and the aspect ratio, $\Gamma = L_z/d$, where L_z is the axial dimension of the domain and d is the gap width, $d = R_o - R_i$. The inner- and outer-cylinder Reynolds numbers are defined by $Re_i = U_i d/\nu$ and $Re_o = U_o d/\nu$, where ν is the fluid kinematic viscosity, and U_i and U_o are, respectively, the rotation velocities of the inner and outer cylinders, $U_i = R_i\Omega_i$ and $U_o = R_o\Omega_o$ (Ω_i and Ω_o denote the angular velocities of the inner and outer cylinders, respectively). We also define another Reynolds number, Re, based on the velocity difference of the inner and outer cylinders, $Re = Re_i - Re_o$.

The experimental work of Andereck *et al.* (1986) at a radius ratio $\eta = 0.883$ has provided so far the most comprehensive map of different regimes of counter-rotating Taylor–Couette flow. Besides the laminar regimes (circular Couette flow, wavy vortex flow, spiral vortices, wavy or modulated inter-penetrating spirals) at relatively low inner- and outer-cylinder Reynolds numbers, it is observed that with increasing Reynolds number, intermittent turbulent spots (bursts) appear randomly in the flow, with scales limited in both space and time. In contrast, the space-filling turbulent burst studied by Coughlin & Marcus (1996) is a temporal oscillation of the laminar flow and the turbulence, and is due to a linear instability. As the inner cylinder rotation rate increases, the turbulent spots grow in size (Goharzadeh & Mutabazi 2001), and eventually connect to form a turbulent spiral. The flow then exhibits patterns of alternating turbulent and laminar spiralling regions (so called spiral turbulence) (Coles 1965; Andereck *et al.* 1986; Goharzadeh & Mutabazi 2001; Prigent *et al.* 2002). Spiral turbulence occurs in counter-rotating systems generally with a higher outer-cylinder Reynolds number (Andereck *et al.* 1986). However, it has also been observed with the inner wall at rest or even in cases with both cylinders rotating in the same direction (Coles 1965). The turbulent spiral appears to have no preferential direction of propagation, and may attain a right or a left helicity with equal probability (Goharzadeh & Mutabazi 2001). It is observed that the spiral pattern rotates with approximately the average angular velocity of the two walls, although the difference between the two can become significant when the outer-cylinder Reynolds number becomes large (Coles 1965). As the inner-cylinder Reynolds number increases, bands of turbulent spirals join together and the entire flow appears turbulent, with no apparent large-scale structures; this is termed featureless turbulence by Andereck *et al.* (1986). The value of the radius ratio significantly influences different flow regimes in the transition diagram. For example, as the radius ratio decreases, spiral turbulence tends to appear at much higher outer-wall Reynolds numbers. With $\eta \approx 0.89$, the minimum outer-cylinder Reynolds number at which spiral turbulence can be observed is about $Re_o \approx -800$ (Andereck *et al.* 1986; Litschke & Roesner 1998), whereas with $\eta \approx 0.79$, this corresponds to $Re_o \approx -7000$. The boundary between featureless turbulence and the other regimes (e.g. spiral turbulence) in the transition diagram tends to shift toward higher Re_o values (for identical Re_i values), see Litschke & Roesner (1998).

In this paper, we focus on the dynamical and statistical features of counter-rotating Taylor–Couette systems (hereinafter referred to as CRTC flow) in the turbulent regime. We consider a range of moderate Reynolds numbers, the largest one being about an order of magnitude higher than those in previous studies (see, e.g. (Antonijoan, Marques & Sanchez 1998; Hoffmann, Lucke & Pinter 2005), at which small-scale azimuthal vortices dominate regions near both cylinder walls. Specifically, we perform three-dimensional direct numerical simulations (DNS) for a radius ratio $\eta = 0.5$ at four inner-/outer-cylinder Reynolds numbers ranging from 500 to 4000, while the condition $Re_i = -Re_o$ is maintained. These approximately correspond to the featureless turbulence or unexplored turbulent regions in the transition diagram of Andereck *et al.* (1986), and the two highest Reynolds numbers in the present study are beyond the range of parameters mapped out in that diagram.

The choice of these parameter values is based on a related study (Dong 2007), in which we have simulated the standard turbulent Taylor–Couette flow (inner cylinder rotating, outer cylinder fixed, hereinafter referred to as the standard configuration or simply TC flow) at Reynolds numbers ranging from 1000 to 8000 for the same radius ratio. The Reynolds numbers in the present study are chosen such that their

values, based on the velocity difference of the inner and outer walls, $Re = Re_i - Re_o$, match those in Dong (2007) (where $Re_o = 0$ for the standard TC flow). This enables a comparison of flow features between the standard and counter-rotating Taylor–Couette turbulence at comparable Reynolds numbers. In Dong (2007), it is observed that in the standard Taylor–Couette system, fine streaks on cylinder walls form intricate herringbone-like patterns, and the flow is dominated by small-scale vortices while large-scale Taylor vortices can barely be discerned from the instantaneous field. It has also been shown that the core of the flow has a constant mean angular momentum. In the present paper, we demonstrate that the counter-rotating Taylor–Couette system shares certain dynamical and statistical features with the standard system, while other characteristics are much modified.

2. Simulation method, convergence and validation

We consider the incompressible flow between two infinitely long concentric cylinders, whose common axis is aligned with the z-axis of the coordinate system. The inner cylinder rotates counterclockwise (when viewed toward the $-z$-direction) at a constant angular velocity Ω_i ($\Omega_i > 0$), while the outer cylinder rotates clockwise at an angular velocity Ω_o ($\Omega_o < 0$). All the length variables are normalized by the cylinder gap d, and the velocity components by the inner wall rotation velocity $U_i = \Omega_i R_i$, and the pressure by ρU_i^2, where ρ is the fluid density.

To solve the three-dimensional Navier–Stokes equations we employ a Fourier spectral expansion of flow variables along the cylinder axis (z-direction), assuming a periodicity of the flow at $z = 0$ and $z = L_z$ (L_z is the axial dimension of the computational domain), and a spectral element discretization (Karniadakis & Sherwin 2005) of the annular domain in (x, y)-planes. We integrate the Navier–Stokes equations in time employing a stiffly stable scheme with a third-order temporal accuracy, and the pressure is computed by solving a Poisson-type equation (Karniadakis, Israeli & Orszag 1991). Dirichlet boundary conditions are employed on the inner and outer cylinder walls to reflect their respective rotation velocities. Parallel computation is through a multi-level parallelization framework (Dong & Karniadakis 2004) and implemented using the message passing interface (MPI). The above scheme has been used previously to study the standard Taylor–Couette turbulence (with fixed outer cylinder) (Dong 2007), high-Reynolds-number turbulent bluff-body flows (Dong & Karniadakis 2005; Dong *et al.* 2006), and vortex-induced vibrations (Dong, Triantafyllou & Karniadakis 2008).

We consider the flow at four Reynolds numbers, $Re_i = -Re_o = 500$, 1500, 2500 and 4000, for a radius ratio $\eta = 0.5$. Note that in all the simulation cases, we have maintained the condition $Re_i = -Re_o$. The axial dimension of the domain is varied between $L_z/d = \pi$ and 2π. We have conducted extensive grid-refinement tests by varying the element order and the number of Fourier planes. We employ a spectral element mesh with 400 quadrilateral elements in the (x, y)-planes, and the element order is varied between 7 and 10, with over-integration (Dong 2007). In the axial direction, we employ 128 to 256 Fourier grid points (64 to 128 Fourier modes), with 3/2-dealiasing. Table 1 summarizes the grid resolution studies at $Re_i = -Re_o = 4000$. It shows the time-averaged mean torque coefficients on the inner and outer cylinder walls with different grid resolutions. The mean torque coefficient is defined as

$$C_T = \frac{\langle T \rangle}{0.5\pi\rho U_i^2 R_i^2 L_z}, \tag{2.1}$$

Cases	N_z	P	L_z/d	C_{Tinner}	C_{Touter}
A	128	8	π	−0.0271	0.0271
B	192	8	1.5π	−0.0272	0.0273
C	256	7	2π	−0.0272	0.0272
D	256	8	2π	−0.0273	0.0272
E	256	9	2π	−0.0272	0.0272
F	256	10	2π	−0.0272	0.0272

TABLE 1. Grid resolution studies at $Re_i = -Re_o = 4000$. N_z, number of Fourier planes in axial direction; P, element order; C_{Tinner}, mean torque coefficient on inner cylinder wall; C_{Touter}, mean torque coefficient on outer cylinder wall.

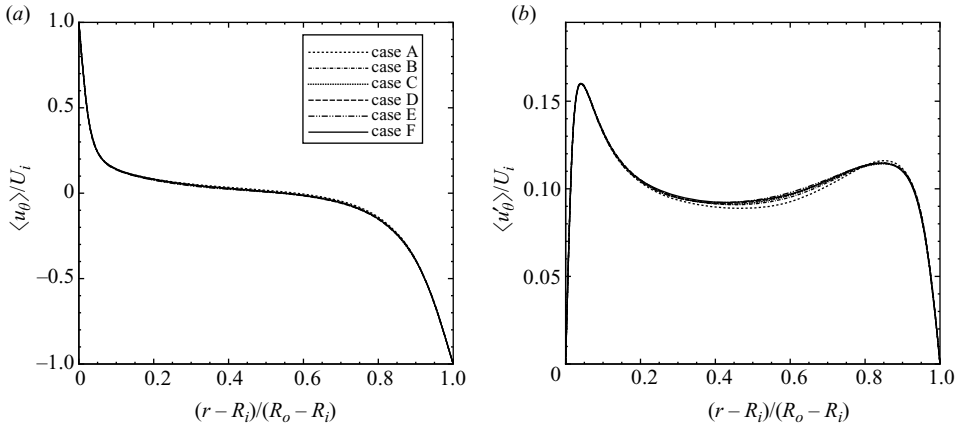

FIGURE 1. Convergence studies ($Re_i = -Re_o = 4000$). Comparison of profiles of (a) the mean azimuthal velocity $\langle u_\theta \rangle$ and (b) the root-mean-square fluctuation azimuthal velocity u'_θ, with different grid resolutions. r is the radial coordinate. Labels of different cases correspond to those in table 1.

where $\langle T \rangle$ is the time-averaged torque value on cylinder walls. The total degrees of freedom in the system has been increased by nearly six times from case A to case F. The torque coefficient is observed to fluctuate slightly (variation less than 0.5 %) at low resolutions and converge to its final value. Comparison of cases A, B and D also demonstrates a general insensitivity of the torque to the axial dimension of the domain.

Figure 1 further demonstrates the convergence of the simulation results with a comparison of profiles of statistical quantities from different grid resolutions at $Re_i = -Re_o = 4000$. In figure 1(a), we plot profiles of the mean azimuthal velocity (normalized by the inner-cylinder rotation velocity), averaged both in time and in the axial and azimuthal directions, as a function of the radial coordinate at various grid resolutions. The mean velocity profiles with different resolutions essentially collapse into one curve, suggesting the grid independence of the results. In figure 1(b), we compare profiles of the root-mean-square (r.m.s.) fluctuation azimuthal velocity (averaged both in time and along the axial and azimuthal directions, and normalized by the inner-cylinder rotation velocity) for different grid resolutions. In the near-wall regions, the profiles for different cases collapse into one. Toward the middle of the gap, some minor differences in the profiles for different cases can be observed; there

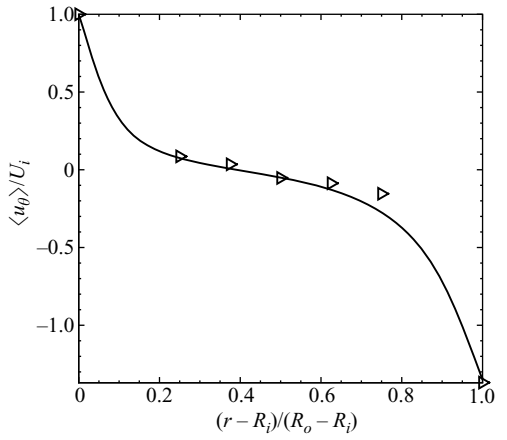

FIGURE 2. Comparison of mean azimuthal velocity profiles between —, the present simulation and ▷, the experiment of Vaezi *et al.* (1997) at $(|Re_i| + |Re_o|)/2 = 1500$ for a radius ratio $\eta = 0.89$.

is a slightly larger difference between the profile from case A and those of the other cases in the middle of the gap and at the peak location near the outer cylinder, while essentially no difference can be discerned between cases with relatively high resolutions (e.g. cases D to F). Both the torque data (table 1) and the statistics data (figure 1) have demonstrated the convergence of the present simulation results.

Our application code has been validated for turbulent Taylor–Couette flows in a previous work (Dong 2007), and also extensively for other turbulence problems such as the bluff-body flows (Dong *et al.* 2006). In Dong (2007), we have compared the computed torque values on the cylinders (standard Taylor–Couette configuration) for Reynolds numbers ranging from 1000 to 8000 with those determined from the experiments of Wendt (1933), Bilgen & Boulos (1973) and Racina & Kind (2006); we have also compared the mean velocity distribution in the gap from the simulations with the experimental data of Smith & Townsend (1982). Very good agreements have been observed in these comparisons. A survey of literature indicates that the experimental data for counter-rotating Taylor–Couette turbulence in the range of Reynolds numbers reachable by DNS (and hence can be used for validating simulations) turns out to be scarce. As a further validation, here we compare our simulations with the experiment of Vaezi, Oh & Aldredge (1997) which was performed for the counter-rotating Taylor–Couette flow in the turbulent regime (figure 2). Note that the experiment of Vaezi *et al.* (1997) was for a radius ratio $\eta = 0.89$ and an inner-/outer-cylinder Reynolds-number ratio $Re_o/Re_i = -1.4$, which were different from the parameters in our simulations. For the purpose of comparison, we have conducted simulations with the above parameter values from the experiment. In figure 2, we compare the profiles of the mean azimuthal velocity (normalized by the rotation velocity of the inner cylinder) at Reynolds number $(|Re_i| + |Re_o|)/2 = 1500$ from our simulation and the experiment of Vaezi *et al.* (1997). The experimental data are only available at a few points around the middle of the gap, in addition to the two points at the walls. The computed profile agrees with the experimental data reasonably well. The slightly larger discrepancy between the simulation and the experiment at the data point toward the outer cylinder may be related to a small

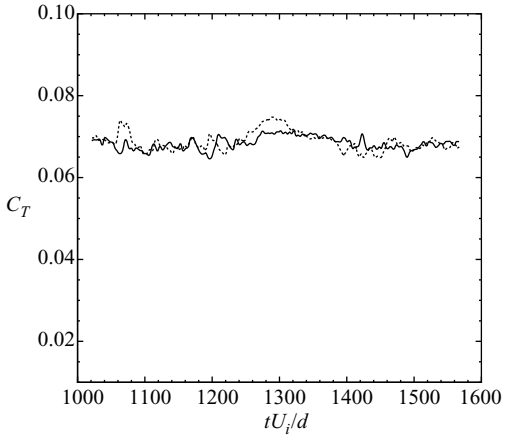

FIGURE 3. Time histories of instantaneous torque coefficients C_T on —, the inner and . . ., outer cylinders at $Re_i = -Re_o = 500$. The torque on the inner cylinder has been made negative in the plot. t denotes time.

mean axial velocity present in the experiment (Vaezi *et al.* 1997) owing to its set-up (no mean axial velocity in the simulations).

3. Dynamical features

We report results of the flow at statistically stationary states only. For this purpose, we have monitored the signals of the instantaneous torques on the inner and the outer cylinders. An example of such signals has been shown in figure 3, in which we plot time histories of the instantaneous torque coefficients (see (2.1), with the mean torque replaced by the instantaneous torque) of the inner and outer cylinders at $Re_i = -Re_o = 500$. While the fluctuations are indicative of the highly dynamical nature of the flow, they are all around some mean value. The constancy of the mean torque suggests that the flow is in a statistically stationary state. For each Reynolds number simulated in this study, we ensure that the flow has reached a statistically stationary state before the flow statistics are accumulated or other characteristics are investigated. All results presented below are for statistically stationary states.

Figure 4 shows contours of the instantaneous azimuthal velocity in a nearly cylindrical surface close to the inner cylinder (at a distance about $0.125d$) for the four Reynolds numbers considered, providing an overview of the instantaneous flow features (side view). Bright regions indicate higher (or more positive) azimuthal velocities, and dark regions indicate lower (or more negative) azimuthal velocity values. At $Re_i = -Re_o = 500$, azimuthal stripes of high velocities (bright regions) can be observed with a fairly regular spacing, approximately $1.1d$ on average, along the axial direction. These are the outflow boundaries of Taylor vortices, which pump high-speed fluids away from the inner cylinder in these regions. Disturbance to the regular pattern of high-velocity stripes can be observed; see figure 4(a) at the lower half of the cylinder. As the Reynolds number increases to 1500 and 2500, structures with smaller scales have emerged in the system, in addition to the high-velocity striped regions which have become increasingly irregular (e.g. appearing broken or forked) with decreased axial spacings. At $Re_i = -Re_o = 4000$ the flow appears to be permeated with the small-scale structures. The pattern of high-speed striped regions

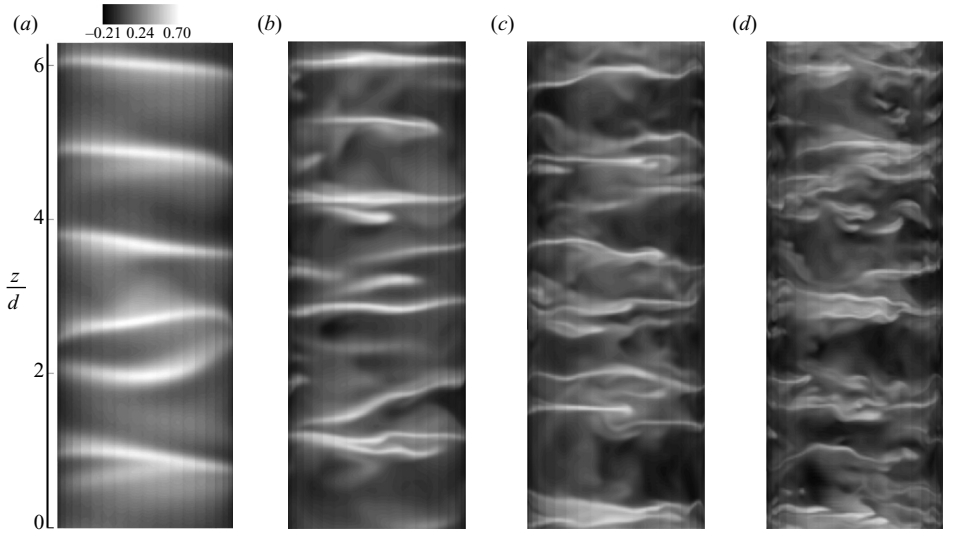

FIGURE 4. Contours of instantaneous azimuthal velocity in a nearly cylindrical surface (at a distance approximately $0.125d$ from the inner cylinder) at Reynolds numbers (*a*) $Re_i = -Re_o = 500$, (*b*) 1500, (*c*) 2500, and (*d*) 4000.

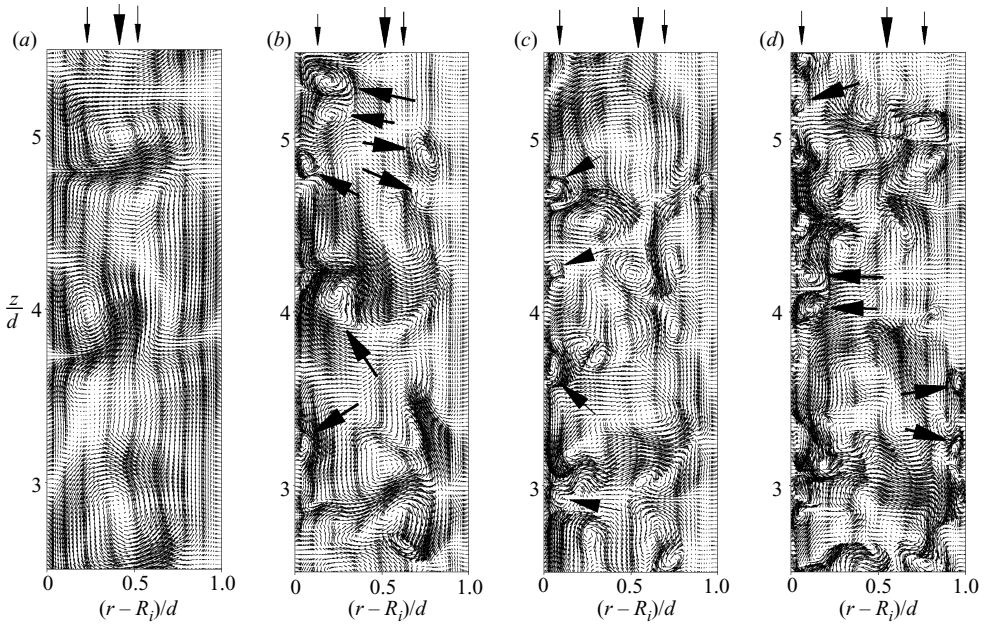

FIGURE 5. Patterns of instantaneous velocity fields in a radial-axial plane at Reynolds numbers (*a*) $Re_i = -Re_o = 500$, (*b*) 1500, (*c*) 2500, and (*d*) 4000. Above each plot the larger arrow indicates the location of the surface with zero mean azimuthal velocities, and the smaller arrows mark the boundaries of high-velocity-gradient layers near the cylinder walls (see § 4).

typical of lower Reynolds numbers has become increasingly less obvious, and highly irregular zones with relatively high or low azimuthal velocities can be identified.

In order to understand the small-scale structures observed in figure 4, we now look into the instantaneous velocity patterns. Figure 5 shows snapshots of the instantaneous

velocity fields in a radial–axial plane (r, z)-plane, where r is the radial coordinate) at Reynolds numbers $Re_i = -Re_o = 500$, 1500, 2500 and 4000. A time-averaged mean velocity field will be shown in § 4. In these plots, the inner and outer cylinder walls, respectively, correspond to $(r - R_i)/d = 0.0$ and 1.0. Note that the velocity vectors have been plotted on the quadrature points of the spectral elements. Because the quadrature points are non-uniformly distributed within an element (finer near boundaries, coarser toward middle of an element) and the sizes of spectral elements are also non-uniformly distributed in the cylinder gap (finer near cylinder walls, coarser toward the middle of the gap), clustering of the quadrature points (and hence the clustering of velocity vectors) induces apparent vertical 'stripes' in the plots.

At $Re_i = -Re_o = 500$, pairs of counter-rotating Taylor vortices can be observed, with a fairly regular spacing in the axial direction. Their outflow boundaries contain the high-speed fluid carried away from the inner cylinder wall, which accounts for the stripes of high-velocity regions in figure 4(*a*). A comparison with the standard Taylor–Couette configuration (Dong 2007) at the same $Re = Re_i - Re_o = 1000$ (TC: $Re_i = 1000$; CRTC: $Re_i = -Re_o = 500$) reveals notable differences. In the standard configuration, the Taylor vortices are observed to fill out the entire gap (Dong 2007); in contrast, in the counter-rotating configuration they appear in size, albeit commensurate to, somewhat smaller than the gap width, and their induced fluid motions tend to be confined to regions in the middle of the gap or near the inner cylinder. A similar observation has been made at lower Reynolds numbers ($Re_i, -Re_o \sim 100$) by others (Hristova *et al.* 2002; Hoffmann *et al.* 2004). Note that in the counter-rotating Taylor–Couette flow there exists a cylindrical surface in the gap with a zero mean azimuthal velocity; we use R^* to denote the radial coordinate of this surface, i.e. $\langle u_\theta \rangle (R^*) = 0$, where $\langle u_\theta \rangle$ is the azimuthal velocity averaged over time and along the axial and azimuthal directions. In figure 5, the larger arrow above each plot marks the location of this zero-velocity surface, and the smaller arrows mark the boundaries of high-velocity-gradient regions near the two walls which will be discussed in detail in § 4. Hoffmann *et al.* (2004) observe that Taylor vortices are restricted not to extend significantly beyond R^* since, based on the Rayleigh criterion (Rayleigh 1916) (valid for inviscid and axisymmetric flows), radial momentum transport is suppressed by opposite pressure gradients for regions outside this location.

As the inner-/outer-cylinder Reynolds number increases to 1500, Taylor vortices diminish notably in size, and their axial spacing has become much less regular. In addition, azimuthal vortices with scales notably smaller than the gap width emerge at the inner cylinder wall, as well as in regions not far from the outer cylinder. In figure 5(*b*), we have marked several such small-scale vortices using arrows. At $Re_i = -Re_o = 2500$, the Taylor vortices, typical at lower Reynolds numbers, can no longer be observed from the instantaneous flow patterns. The flow field comprises numerous small-scale vortices, predominantly located at the inner cylinder (see the arrows in figure 5*c*) and in the bulk of the gap; they can barely be observed in regions very close to the outer cylinder. The small-scale vortices collectively appear to be clustered around several axial locations, with regions in between relatively free of small-scale vortices. At $Re_i = -Re_o = 4000$, small-scale vortices appear to be permeated throughout the gap. They can especially be observed at and in regions near the outer cylinder wall (see vortices marked by arrows near the outer cylinder in figure 5*d*), which are generally free of vortices at lower Reynolds numbers. However, the population of vortices at the inner cylinder appears to be considerably larger than at the outer one.

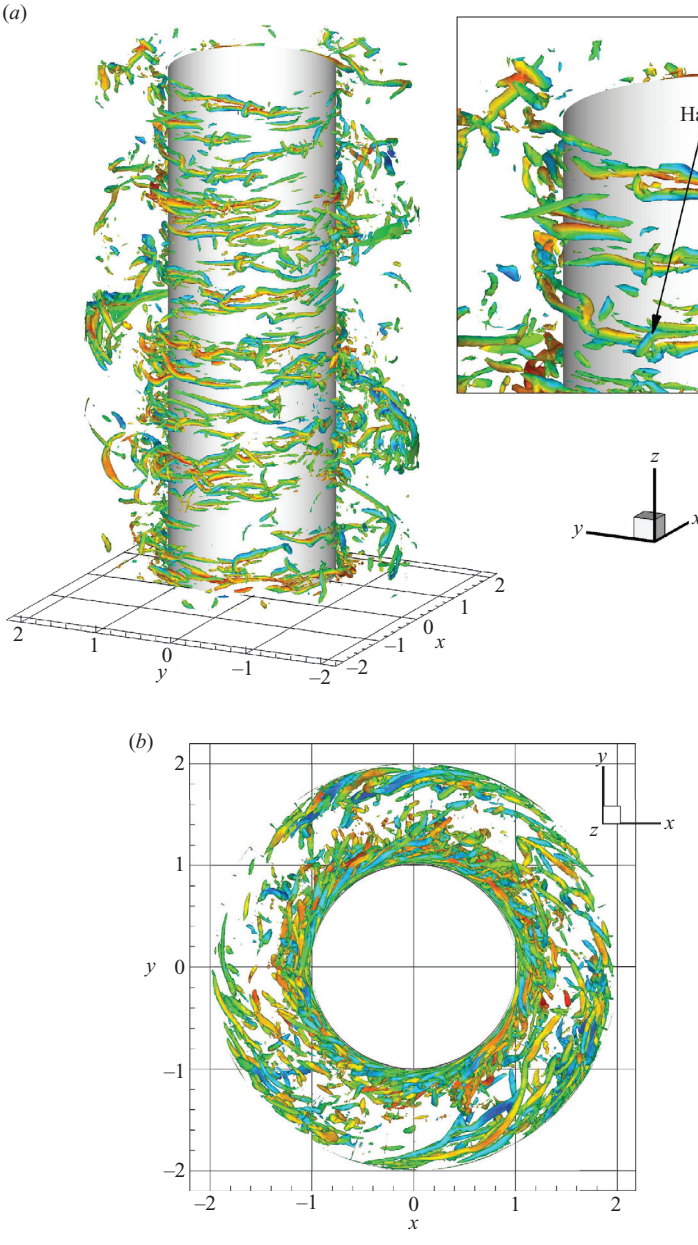

FIGURE 6. Iso-surface of instantaneous λ_2 (the intermediate eigenvalue in Jeong & Hussain (1995) vortex identification method) at $Re_i = -Re_o = 4000$: (*a*) perspective view, the inset being an enlarged view near the upper end of the inner cylinder; (*b*) top view. Colour contours of the radial velocity are shown on the λ_2 iso-surface: red, positive radial velocity; blue, negative radial velocity. The inner cylinder is also shown in the plot.

The above observations for the counter-rotating system and those in Dong (2007) for the standard configuration suggest that it is a characteristic common to both standard and counter-rotating Taylor–Couette flows that with increasing Reynolds number the large-scale Taylor vortices (typical at low Reynolds numbers) cease to exist in the instantaneous sense, i.e. they can no longer be observed from the instantaneous flow

patterns. As the Reynolds number increases, the prevailing structure is the azimuthal vortices with scales much smaller than the gap width. In standard Taylor–Couette flows, it has been shown that the small-scale vortices originate at the inner cylinder wall and around the outflow boundaries of Taylor vortices (Wei *et al.* 1992; Dong 2007). For the counter-rotating configuration, the above point is not quite obvious from the present data. The small-scale vortices seem to appear first at the inner wall, because at $Re_i = -Re_o = 1500$ the outer wall is free of vortices whereas they can already be observed at the inner wall. However, whether the small-scale vortices originate from the outflow boundaries of Taylor vortices is not clear from the data. Compared to the plane Couette flow, we note the strong asymmetry of flow features here between the inner and the outer cylinder walls. This is reflected from the general confinement of Taylor vortices to the inner portion of the gap at low Reynolds numbers and the considerable difference in the population of small-scale vortices at the two walls as the Reynolds number increases.

To explore the structural characteristics of the small-scale vortices in three-dimensional space, we employ the method of Jeong & Hussain (1995) for vortex identification. In figure 6, we visualize the vortices at $Re_i = -Re_o = 4000$ by plotting the iso-surface of $\lambda_2 = -7.0$, where λ_2 is the intermediate eigenvalue of the tensor $\boldsymbol{S}\cdot\boldsymbol{S} + \boldsymbol{\Omega}\cdot\boldsymbol{\Omega}$ ($\boldsymbol{S}$ and $\boldsymbol{\Omega}$, respectively, denote the symmetric and anti-symmetric parts of the velocity gradient tensor). figure 6(*a*) shows a perspective view, the inset being an enlargement around the top end of the cylinder, and figure 6(*b*) is a top view. To provide the sense of rotation of the vortices, we have plotted contours of the instantaneous radial velocity u_r on the λ_2 iso-surface. Red indicates a positive radial velocity (i.e. flow from inner cylinder to outer cylinder), and blue indicates a negative one. For an azimuthally elongated vortex, we can usually observe a positive radial velocity (red) on one side of the vortex tube and a negative radial velocity (blue) on the other; the sense of its rotation can be determined as a result. The figure demonstrates numerous small-scale vortices in the flow, extending in general along the azimuthal direction in three-dimensional space. Nearly all the azimuthal vortices seem to appear in pairs. The two vortices in a pair have opposite senses of rotation (i.e. counter-rotating), and their strengths (or sizes) can differ considerably (figure 6*a*). Instantaneously, the vortices appear to originate from the inner or the outer cylinder, stretch azimuthally, and extend away from the wall to the core of the gap (figure 6*b*); the majority of vortices are distributed in regions near either the inner cylinder or the outer one, and the middle region of the gap is relatively void of vortices. In some instances, the pair of azimuthal counter-rotating vortices appears to form the legs of a hairpin-like vortex. For example, several hairpin-like vortices can be clearly identified on the inner cylinder wall from the inset of figure 6(*a*). Hairpin vortices have been observed in turbulent channels and flat-plate boundary layers, and been considered as a promising conceptual model for basic near-wall structures of turbulence (Robinson 1991; Adrian 2007). In the counter-rotating Taylor–Couette system studied here, we note that the majority of small-scale vortices appear to be azimuthally elongated vortices and not connected with a hairpin-like vortex.

One of the most intriguing features of turbulent Taylor–Couette flows in a standard configuration is the presence of near-wall streaks that form herringbone-like patterns. The herringbone-like streaks were first observed in a visualization study (Barcilon *et al.* 1979), and have also been observed in direct numerical simulations (Dong 2007). Barcilon *et al.* (1979) show flow photographs of fine streaks (aluminium particles) on the outer cylinder wall that tilt alternately at small angles with respect to the planes normal to the cylinder axis. Dong (2007) demonstrates that Herringbone streaks

start to appear on the walls as the Reynolds number reaches a threshold value, and that they are initially distributed in banded regions concentrating on certain axial locations. With increasing Reynolds number, it is observed that the streaks spread over the entire cylinder surface and become less coherent (persisting for a shorter time), and their population increases dramatically. The studies of both Barcilon *et al.* (1979) and Dong (2007) are for a standard Taylor–Couette configuration.

A natural question arises as to whether the existence and the characteristics of herringbone streaks carry over to the counter-rotating Taylor–Couette systems. In light of this question, we next investigate the spatial–temporal characteristics of the flow. Figure 7 shows contours of the instantaneous azimuthal velocity in the spatial–temporal (z, t)-plane for Reynolds numbers ranging from $Re_i = -Re_o = 500$ to 4000. The velocity data were collected along a fixed line parallel to the cylinder axis and located near the inner cylinder wall (at a distance $0.033d$). The contour levels of the azimuthal velocity range from $0.45U_i$ to $0.9U_i$ in these plots, and the regions with contours are associated with a higher azimuthal velocity than the ambient (blank) ones. At $Re_i = -Re_o = 500$, distinct high-speed regions marked by the contour lines correspond to the outflow boundaries of Taylor vortices (see also figures 5*a* and 4*a*). Instabilities localized in both space and time can be clearly observed. However, no obvious pattern can be discerned at this Reynolds number. As the Reynolds number increases to 1500 and above, interesting herringbone-like patterns of streaks are observed. The streaks appear to share certain characteristics with those observed in the standard Taylor–Couette configuration (Barcilon *et al.* 1979; Dong 2007). For example, they tilt alternately at small angles with respect to the (x, y)-plane; with the increase of Reynolds number, the streaks tend to be finer and more closely packed, and their population increases dramatically. Some differences are also noted despite these similarities. In the standard Taylor–Couette configuration, the herringbone streaks are distributed in banded regions along the axial direction (Dong 2007), which are disjoint when the streaks start to appear and are quite evident even at high Reynolds numbers. On the other hand, in a counter-rotating system, it is not obvious that the streaks are distributed in banded regions, especially as the Reynolds number increases. They appear to be on the entire cylinder wall. For example, at the same $Re = Re_i - Re_o = 3000$ ($Re_o = 0$ for standard Taylor–Couette flow) the herringbone streaks in the standard configuration are distributed in disjoint bands along the axial direction (Dong 2007), whereas this is apparently not quite the case in the counter-rotating configuration (figure 7*b*). Comparisons of the standard configuration and the counter-rotating configuration at the same $Re = Re_i - Re_o$ values also indicate that the streaks in the counter-rotating system tend be more coherent (i.e. persisting longer in time) and less populous.

We next investigate the spectral characteristics of velocity fluctuations. Figure 8 shows a comparison of the Fourier power spectra of the axial velocity near the inner cylinder (at a distance $0.108d$) at different Reynolds numbers. The spectra were computed based on the time histories of velocity at certain points in the flow domain, and have been averaged along the axial direction over points with the same radial and azimuthal coordinates. The spectra at all four Reynolds numbers exhibit a broadband distribution typical of a turbulent power spectrum, which indicates that the flow has become turbulent at all four Reynolds numbers. At $Re_i = -Re_o = 500$, although the velocity fluctuations are quite weak (which can be two orders of magnitude weaker than at $Re_i = -Re_o = 1500$ at higher frequencies), the spectrum has nonetheless retained characteristics of a turbulent spectrum. At very low frequencies ($fd/U_i < 0.1$), the spectra for $Re_i = -Re_o = 1500$, 2500 and 4000 essentially coincide with one

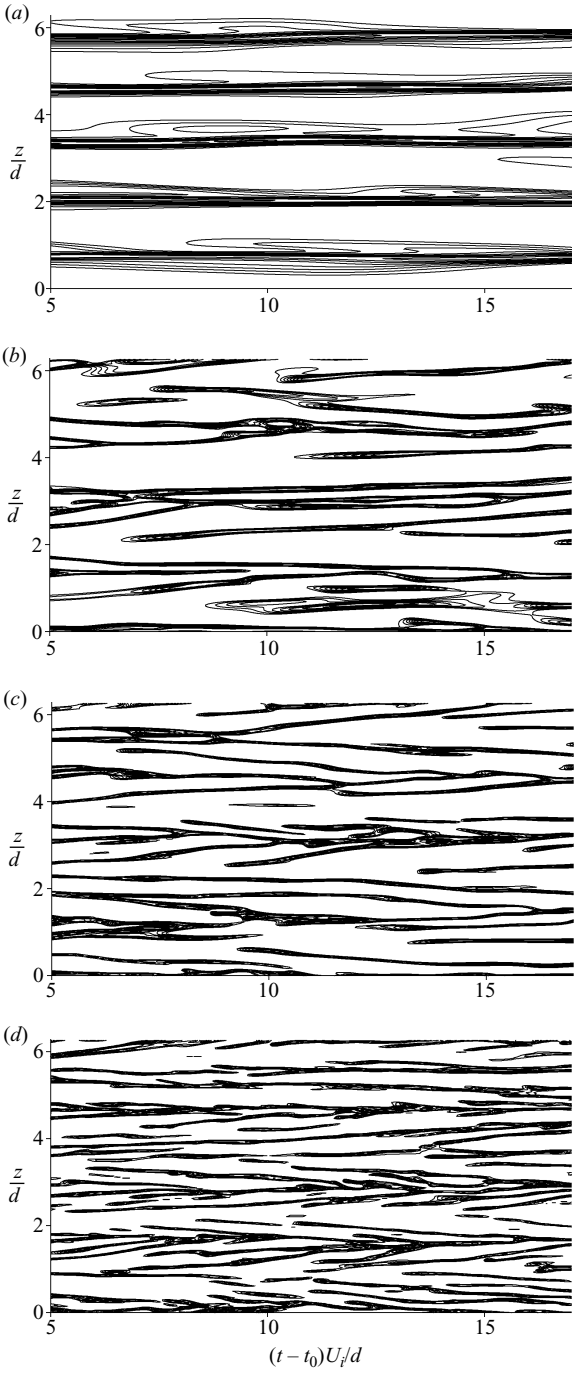

FIGURE 7. Spatial–temporal contours of the azimuthal velocity along a fixed line that is parallel to the z-axis and near the inner cylinder wall (at a distance $0.033d$): (*a*) $Re_i = -Re_o = 500$, (*b*) 1500, (*c*) 2500, and (*d*) 4000. t_0 is an arbitrary instant in time.

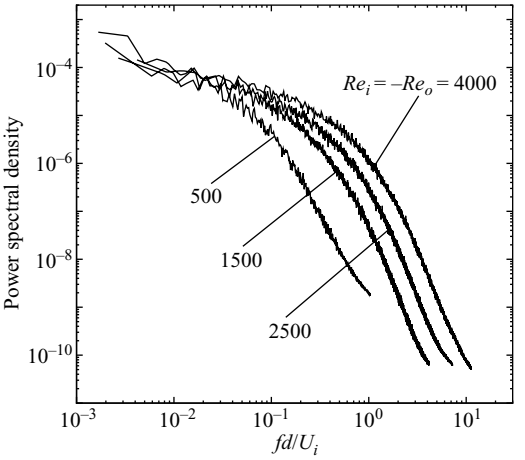

FIGURE 8. Power spectra of the axial velocity at a distance $0.108d$ away from the inner cylinder at different Reynolds numbers. f denotes frequency.

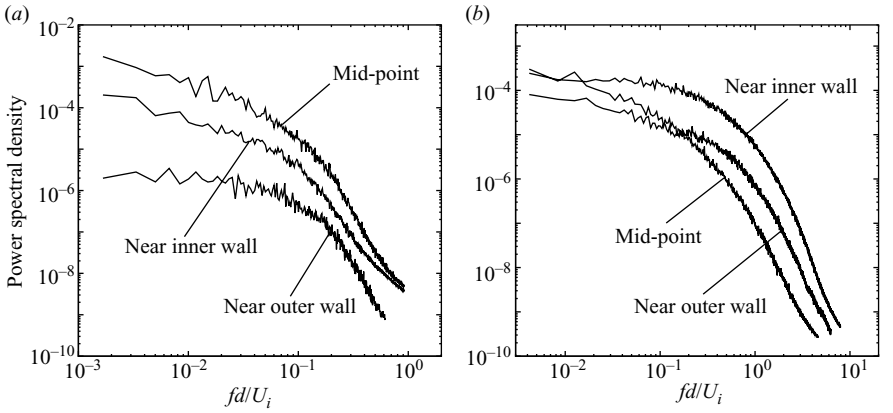

FIGURE 9. Power spectra of the azimuthal velocity in the middle of the gap and at two other locations near the inner and outer cylinder walls (at a distance $0.033d$): (*a*) $Re_i = -Re_o = 500$ and (*b*) 4000. In (*b*), the curves for the mid-point and the point near the outer wall intersect with each other.

another, indicating that on temporal scales about $10d/U_i$ and larger, the intensity of fluctuations for the three Reynolds numbers is comparable. At higher frequencies ($fd/U_i > 0.1$), differences in the power spectral density among various Reynolds numbers become more significant; turbulent fluctuations are substantially stronger at a higher Reynolds number. At frequencies $fd/U_i \geqslant 1.0$, the difference in the power spectral density values between successive Reynolds numbers is nearly an order of magnitude.

Turbulent fluctuations are unevenly distributed in intensity in the domain, and the distribution characteristics differ with the Reynolds number. In figure 9, we compare the power spectra of the azimuthal velocity at three locations, the mid-point of the gap and two near-wall locations (at a distance $0.033d$), at Reynolds numbers $Re_i = -Re_o = 500$ (figure 9*a*) and 4000 (figure 9*b*). At $Re_i = -Re_o = 500$, we observe more energetic fluctuations (higher power spectral density) in the middle region of the gap than near the cylinder walls. This characteristic is reversed as

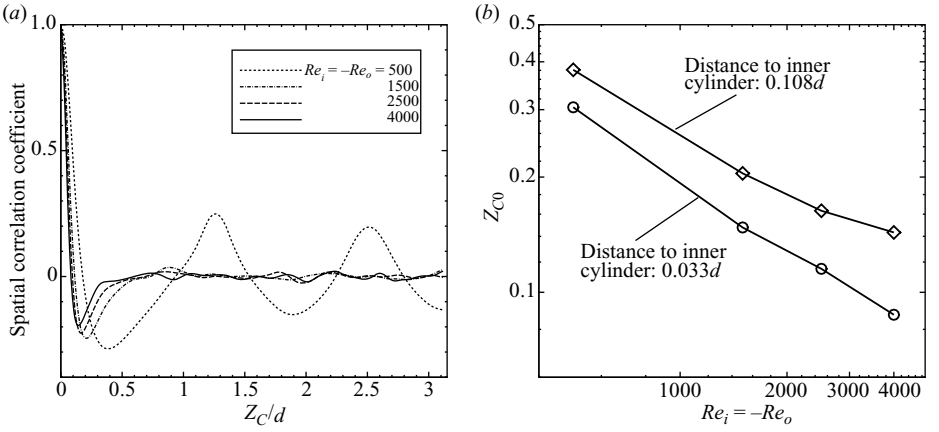

FIGURE 10. Spatial correlations: (a) two-point autocorrelation function of the fluctuation radial velocity versus the axial separation of the two points, Z_c, for a location near the inner cylinder (at a distance $0.108d$); (b) axial separation that corresponds to the minimum correlation coefficient, Z_{C0}, as a function of Reynolds number.

the Reynolds number increases. With increasing Reynolds number, the intensity of turbulent fluctuations near cylinder walls, especially near the inner cylinder, increases substantially and surpasses that of the middle region of the gap. figure 9(b) shows that at $Re_i = -Re_o = 4000$, the most energetic fluctuations are observed near the inner cylinder. Comparison between the gap mid-point and the point near the outer cylinder indicates that high-frequency fluctuations are stronger near the outer cylinder, whereas at low frequencies ($fd/U_i \lesssim 0.2$) it is relatively stronger at the mid-point of the gap. These distribution characteristics are related to the vortex distributions in the flow. At a low Reynolds number such as $Re_i = -Re_o = 500$, Taylor vortices dominate the middle region and the inner portion of the gap (figure 5a). This apparently results in stronger fluctuations in the middle of the gap than in the near-wall regions. As the Reynolds number increases, small-scale vortices emerge and are predominantly distributed near both cylinder walls, especially at the inner cylinder, while the middle region of the gap is comparatively vortex-free (figure 6b). This gives rise to stronger turbulent fluctuations in near-wall regions than in the middle of the gap.

We next study the spatial and temporal correlations of the velocity fluctuations. figure 10(a) shows the spatial two-point autocorrelation coefficient of the fluctuation radial velocity as a function of the axial separation (Z_c) between the two points at different Reynolds numbers. The spatial correlation coefficient is defined for two points separated by a distance Z_c in the axial direction by the following expression

$$R_{rr}(Z_c; r) = \frac{\overline{u_r'(r, \theta, z, t) u_r'(r, \theta, z + Z_c, t)}}{\overline{u_r'^2(r, \theta, z, t)}}, \tag{3.1}$$

where the bar denotes the averaging over time and along the azimuthal and axial directions. The fluctuation radial velocity u_r' is defined by $u_r'(r, \theta, z, t) = u_r(r, \theta, z, t) - U_r(r, \theta, z)$, where $U_r(r, \theta, z)$ is the time-averaged mean of the instantaneous radial velocity $u_r(r, \theta, z, t)$. The correlation distribution in figure 10(a) is for a location $0.108d$ away from the inner cylinder. At $Re_i = -Re_o = 500$, the two-point autocorrelation exhibits large variations about the zero value with increasing axial separation, which is indicative of the regular Taylor vortex patterns at this Reynolds number (figures 4a

and 5*a*). As the Reynolds number increases to $Re_i = -Re_o = 1500$ and above, velocity fluctuations at any two points separated by about $0.5d$ or more in the axial direction completely lose correlation. As the axial separation between the two points increases from zero, the autocorrelation coefficient decreases and rapidly becomes negative. This negative region in the autocorrelation function is due to the near-wall small-scale vortices (figure 5), and in the case of $Re_i = -Re_o = 500$, the Taylor vortices. The radial velocity fluctuations tend to be negatively correlated across an azimuthal vortex tube. Therefore, the axial separation that corresponds to the minimum correlation (negative peak), Z_{C0}, provides a measure for the characteristic size of the near-wall azimuthal vortices. We have determined Z_{C0} for different Reynolds numbers. In Figure 10(*b*), we plot Z_{C0} as a function of the Reynolds number at two locations, respectively, with distances $0.033d$ and $0.108d$ to the inner cylinder wall. Evidently the axial separation that corresponds to the minimum correlation coefficient decreases with increasing Reynolds number, indicating a marked decrease in the size of near-wall azimuthal vortices as the Reynolds number increases. The curves suggest that the dimension of the near-wall vortices approximately scales as a function $\sim Re_i^{\xi}$ (ξ being the slope of the curves), with $\xi \approx -0.62$ at a distance $0.033d$ from the inner wall and slightly increasing at locations farther away from the wall.

Taylor microscales can be determined based on the spatial correlation functions. The longitudinal Taylor microscale (Pope 2000) is defined by $\lambda_f(r) = [-(1/2)(d^2R_{zz}(Z_c;r)/dZ_c^2)|_{Z_c=0}]^{-1/2}$, where $R_{zz}(Z_c;r)$ is the spatial two-point autocorrelation of the fluctuation axial velocity (see (3.1), with the radial velocity u_r replaced by the axial velocity u_z). Similarly, the transverse Taylor microscale can be determined by $\lambda_g(r) = [-(1/2)(d^2R_{rr}(Z_c;r)/dZ_c^2)|_{Z_c=0}]^{-1/2}$, where $R_{rr}(Z_c;r)$ is the spatial autocorrelation of the fluctuation radial velocity (equation (3.1)). We have computed the Taylor microscales at several radial locations, and in figures 11(*a*) and 11(*b*) we plot the distributions of the longitudinal and transverse Taylor microscales across the cylinder gap at various Reynolds numbers. We first note the non-homogeneity of the distribution. The values of Taylor microscales vary substantially across the gap; at Reynolds numbers $Re_i = -Re_o = 1500$ and above, high values are found in the middle of the gap (slightly shifted toward the outer cylinder), and relatively low values can be observed near both walls. The distribution at $Re_i = -Re_o = 500$ exhibits certain 'irregularities'. The transverse Taylor microscale increases monotonically as the radial coordinate increases, unlike the other Reynolds numbers; this is probably due to the very weak fluctuations near the outer wall at this Reynolds number. Comparison of different Reynolds numbers shows that both the longitudinal and the transverse Taylor microscales decrease with increasing Reynolds number. Figure 11(*c*) shows distributions of the Taylor-scale Reynolds number, Re_λ, which is defined by $Re_\lambda(r) = u'(r)\lambda_g(r)/\nu$ (Pope 2000), where u' is the fluctuation velocity magnitude, $u' = \sqrt{\overline{u_r'^2 + u_\theta'^2 + u_z'^2}}$ (u_r', u_θ' and u_z' are, respectively, the fluctuation radial, azimuthal and axial velocities, and the overbar denotes averaging in time and along the axial and azimuthal directions). With the increase of Reynolds number, the values of Taylor-scale Reynolds number increase from around 10 at $Re_i = -Re_o = 500$ to about 50 at $Re_i = -Re_o = 4000$. At each Reynolds number, highest values of Taylor-scale Reynolds number occur in the middle region of the gap whereas the values in near-wall regions are comparatively low.

Figure 12(*a*) shows the temporal autocorrelation coefficient of the fluctuation radial velocity as a function of the time separation between the two instants, τ, at different Reynolds numbers for a location near the inner cylinder (at a distance $0.033d$). The

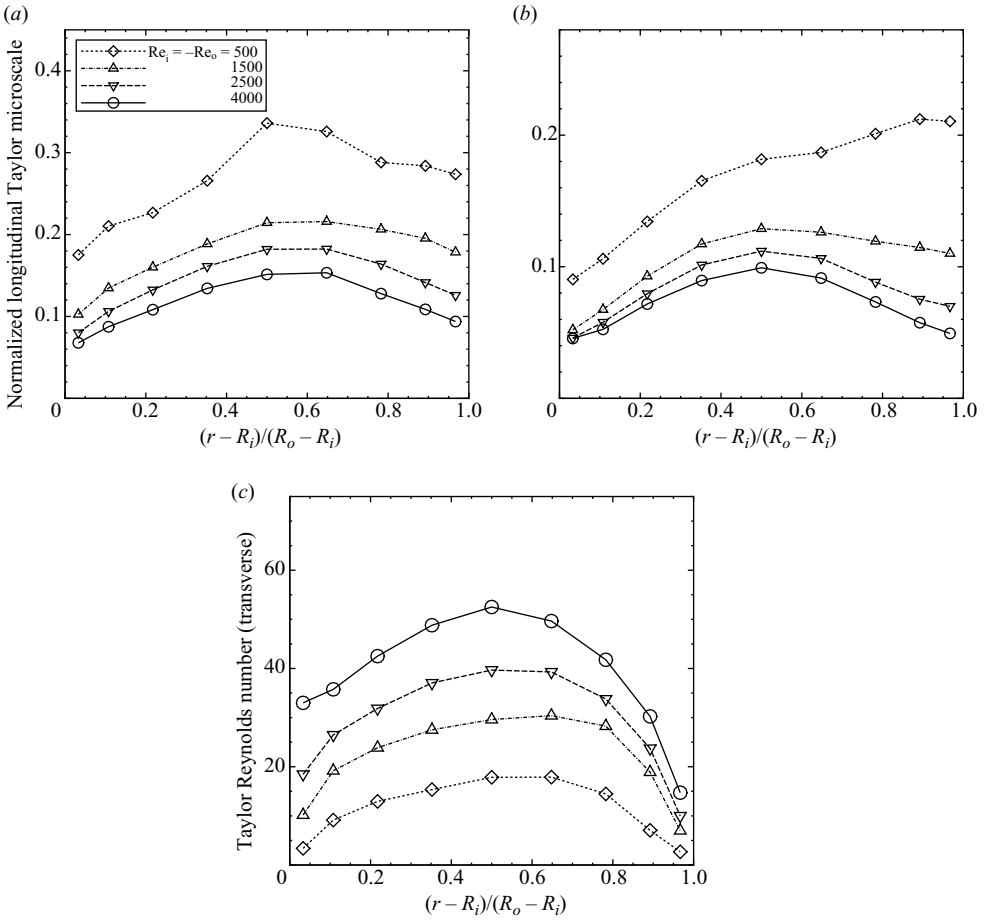

FIGURE 11. Taylor microscales and Taylor-scale Reynolds numbers: distribution of (*a*) longitudinal and (*b*) transverse Taylor microscales (normalized by cylinder gap) and (*c*) the Taylor-scale Reynolds numbers.

temporal autocorrelation coefficient is defined by

$$R_{rr}(\tau; r) = \frac{\overline{u_r'(r, \theta, z, t) u_r'(r, \theta, z, t+\tau)}}{\overline{u_r'^2(r, \theta, z, t)}}, \tag{3.2}$$

where the bar denotes the averaging in time and in the axial and azimuthal directions. The autocorrelation coefficient decreases rapidly as the time separation increases. However, the rate of decrease is quite different at different Reynolds numbers. At Reynolds numbers $Re_i = -Re_o = 1500$ and above, the fluctuation velocity becomes uncorrelated with a relatively short time separation, whereas at $Re_i = -Re_o = 500$ the decrease of the autocorrelation is much slower. The decay time of the autocorrelation function provides a measure of the typical time it takes for an azimuthal vortex to pass a fixed point in space. If the convection velocity of the vortex is known, e.g. by assuming that it is the same as the mean flow velocity, then the decay time is practically a measure of the characteristic 'length' of the vortex. A quantitative measure of the rate of decrease is the integral time scale (Tritton 1988), T_e, defined

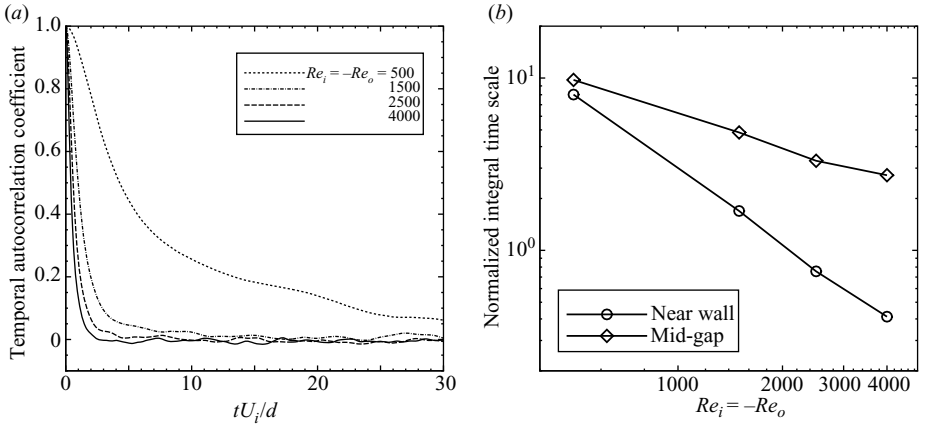

FIGURE 12. Temporal correlations: (*a*) two-point autocorrelation function of the fluctuation radial velocity versus the temporal separation between the two instants, τ; for a location near the inner cylinder (at a distance $0.033d$); (*b*) integral time scale as a function of Reynolds number ○, near-wall; ◇, mid-gap.

by $T_e = \int R_{rr}(\tau; r)\, \mathrm{d}\tau$. In figure 12(*b*), we plot the integral time scale, normalized by d/U_i, as a function of the Reynolds number at two locations: near the inner cylinder wall (at a distance $0.033d$) and in the mid-point of the gap. The integral time scale in the mid-gap is notably larger than near the wall, suggesting a stronger correlation of turbulent fluctuations. The integral time scale decreases with increasing Reynolds number, and scales as a function $\sim Re_i^{\xi}$ (where ξ is the slope of the curves), with $\xi \approx -1.44$ near the wall and $\xi \approx -0.64$ in the middle of the gap.

4. Statistical features

In this section, we investigate the characteristics of flow statistics, with an emphasis on the time-averaged mean field and the root-mean-square (r.m.s.) velocity fluctuations. By averaging the Navier–Stokes equations in time and in the axial and azimuthal directions, Eckhardt, Grossmann & Lohse (2007) observe that in a differentially rotating Taylor–Couette system, the following quantity is a constant across the cylinder gap,

$$J^{\omega} = r^3 \left(\langle u_r \omega \rangle - \nu \frac{\partial \langle \omega \rangle}{\partial r} \right), \tag{4.1}$$

where ω is the angular velocity, and $\langle \cdot \rangle$ denotes the averaging over time and in the axial and azimuthal directions. They refer to J^{ω} as the angular velocity current because it can be interpreted as a conserved transverse current of the azimuthal motion, transporting the angular velocity ω in the radial direction (Eckhardt *et al.* 2007). The first term on the right-hand side of (4.1) represents a 'Reynolds stress' and the second term a viscous derivative of the mean angular velocity. Since different terms can be computed independently, (4.1) can serve as a consistency check of the simulation results. In figure 13, we plot profiles of the individual terms in (4.1), $-r^3 \nu (\partial \langle \omega \rangle / \partial r)$ and $r^3 \langle u_r \omega \rangle$, and their sum, $r^3(\langle u_r \omega \rangle - \nu(\partial \langle \omega \rangle / \partial r))$, all normalized by $U_i^2 d^2$, at Reynolds number $Re_i = -Re_o = 4000$. Indeed, the angular velocity current J^{ω} is essentially a constant across the cylinder gap.

$Re_i = -Re_o$	$4J^\omega/U_i^2R_i^2$	C_T
500	0.0693	0.0686
1500	0.0390	0.0392
2500	0.0324	0.0322
4000	0.0271	0.0272

TABLE 2. Comparison of non-dimensional angular velocity current $J^\omega/(U_i^2R_i^2/4)$ and the mean torque coefficient C_T (equation (2.1)) at different Reynolds numbers.

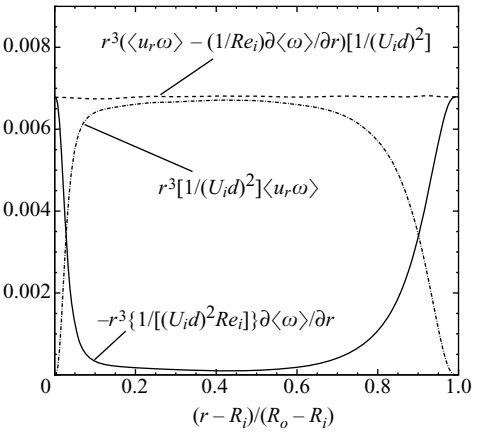

FIGURE 13. Balance of angular velocity current J^ω at $Re_i = -Re_o = 4000$. ω is the angular velocity.

The angular velocity current is also related to the torque on the cylinders, which is provided by the following equation,

$$C_T = \frac{J^\omega}{\frac{1}{4}U_i^2R_i^2}, \tag{4.2}$$

where C_T is the mean torque coefficient defined in (2.1). Both sides of the equation can be determined independently, e.g. C_T by time-averaging the instantaneous torque on the cylinder and J^ω by using (4.1). So equation (4.2) can serve as another consistency check of the simulation data. We have computed these physical parameters, and in table 2 compare both sides of (4.2) as a function of Reynolds number. In the table, J^ω is an average value across the cylinder gap. As expected, the values of the two parameters are essentially the same (with a difference of about 1 % or less). Note that the volume-averaged dissipation rate, $\langle\epsilon\rangle$, is related to the mean torque coefficient C_T by $\langle\epsilon\rangle/U_i^2\Omega_i = C_T\eta^2/(2(1-\eta))$ (Lewis & Swinney 1999), and therefore can be determined from the data in table 2.

Figure 14 shows the time-averaged mean velocity field in a radial-axial plane at $Re_i = -Re_o = 4000$, which can be compared to the instantaneous velocity patterns at the same Reynolds number (figure 5*d*). Instantaneously, small-scale azimuthal vortices dominate the flow and no large-scale vortex patterns can be discerned; the mean flow field, on the other hand, reveals the organized pattern of large-scale Taylor vortices (commensurate to the cylinder gap) underlying the turbulent fluctuations. This indicates that the collective fluid motion induced by the numerous small-scale azimuthal vortices represents that of large-scale Taylor vortices, although Taylor

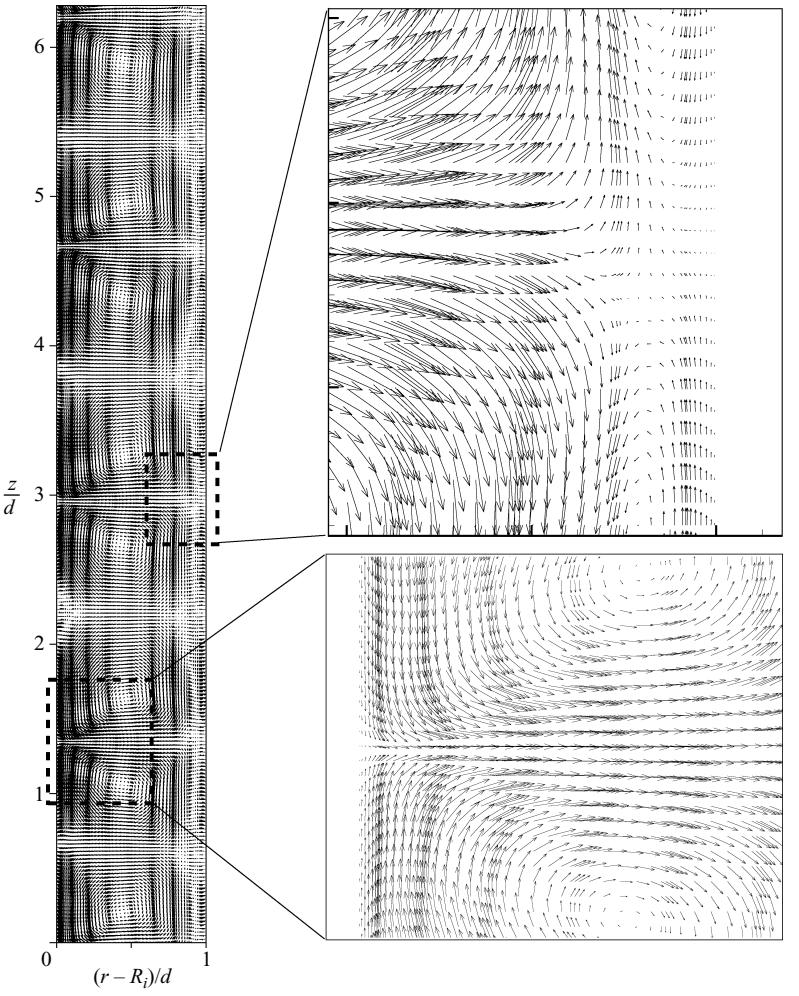

FIGURE 14. Time-averaged mean velocity field in a radial-axial plane at $Re_i = -Re_o = 4000$.

vortices by themselves do not exist in the instantaneous sense at high Reynolds numbers. This appears to be a common characteristic of Taylor–Couette systems, as a similar observation has been made by Dong (2007) for the standard configuration.

Another interesting observation about the mean flow is the existence of a thin layer of fluid near the outer cylinder, whose motion in the radial-axial plane is opposite to that induced by the Taylor vortices; See the inset of figure 14 for a detailed view. As the inner-/outer-cylinder Reynolds number increases from 500 to 4000, the thickness of this fluid layer decreases from $0.18d$ to $0.08d$. The presence of such a fluid layer indicates that at high Reynolds numbers, the large-scale Taylor vortices manifested by the time-averaged field are still confined toward the inner portion of the gap, and in the mean sense their induced fluid motions do not penetrate regions very close to the outer cylinder. At low Reynolds numbers, the confinement of Taylor vortices is quite evident from the instantaneous flow (figure 5*a*). As the Reynolds number increases, this is not apparent. At high Reynolds numbers, Taylor vortices can no longer be observed instantaneously, and the small-scale vortices appear to permeate the entire cylinder gap (figure 5*d*). In fact, they have been predominantly observed

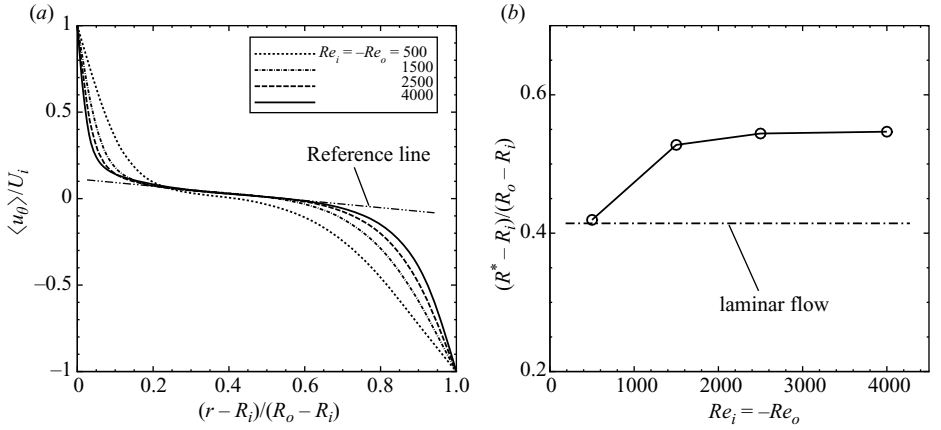

FIGURE 15. Mean flow: (*a*) comparison of mean azimuthal velocity profiles at different Reynolds numbers; (*b*) radial coordinate of the zero velocity surface as a function of Reynolds number. u_θ is the azimuthal velocity and R^* is the radius of zero-velocity surface.

in regions near both cylinder walls (figure 6*b*). This indicates that at high Reynolds numbers, the instantaneous vortices are no longer confined to the inner portion of the gap, unlike at low Reynolds numbers. It is therefore surprising to observe that in the time-averaged-mean sense, the Taylor vortex motions, that is, the motions induced collectively by the small-scale vortices, still cannot penetrate the region very close to the outer cylinder, even though individual small-scale vortices dominate this region instantaneously.

In figure 15(*a*), we compare profiles of the mean azimuthal velocity (u_θ denotes the azimuthal velocity), averaged over time and along the axial and azimuthal directions, at different Reynolds numbers. The velocity has been normalized by the rotation velocity of the inner wall. We first note the asymmetry of the profiles at the cylinder walls, different from plane Couette flows. With the increase of Reynolds number, although the velocity gradients increase at both walls, higher values are always associated with the inner wall. The core of flow (with a slight shift toward the inner cylinder) has quite low azimuthal velocities, nearly zero at Reynolds numbers $Re_i = -Re_o = 1500$ and above. This region of near-zero velocity becomes wider as the Reynolds number increases. The location of the surface with zero azimuthal velocity can be determined from the mean velocity profiles. We have computed the radial coordinate R^* of the zero-velocity surface. In figure 15(*b*), we plot the normalized R^* as a function of Reynolds number, together with the location of the zero-velocity surface in a laminar circular Couette flow with $U_i = -U_o$ and $\eta = 0.5$ plotted as a horizontal line. The radius of the zero-velocity surface at $Re_i = -Re_o = 500$ is nearly the same as (slightly larger than) that of the laminar Couette flow, which is $(R^* - R_i)/(R_o - R_i) = \sqrt{2} - 1$. As the Reynolds number increases (while maintaining the condition $Re_i = -Re_o$), the zero-velocity surface moves outward, and its radius appears to approach a limiting value about $(R^* - R_i)/(R_o - R_i) \sim 0.55$.

To understand why there exists a limiting value for R^* as the Reynolds number increases while the condition $Re_i = -Re_o$ is maintained, we look into the distribution of the mean angular velocity $\langle \omega \rangle$ in more detail. Figure 13 shows that the term $J_\nu^\omega = -r^3 \nu (\partial \langle \omega \rangle / \partial r)$ has a very low value in the core of the flow (with a slight shift toward the inner cylinder), essentially negligible compared to the other term, $r^3 \langle u_r \omega \rangle$. Examination of the J_ν^ω term at different Reynolds numbers indicates that the higher

the Reynolds number, the smaller the percentage contribution of the J_ν^ω term to the total J^ω in the core of the flow. It is therefore reasonable to assume that at sufficiently high Reynolds numbers, $J_\nu^\omega \approx 0$, and hence $\partial\langle\omega\rangle/\partial r \approx 0$, in the core; It follows that $\langle\omega\rangle$ is a constant, and the mean azimuthal velocity becomes a linear function, i.e. $\langle u_\theta\rangle \sim ar$ (where a is a constant). This indicates that at sufficiently high Reynolds numbers, the profile of the mean azimuthal velocity approaches a straight line in the core of flow. This trend indeed has been demonstrated by the velocity profiles in figure 15(a); see the straight reference line in the plot. The intersection of this limiting straight line and the line $\langle u_\theta\rangle = 0$ determines the limiting location of the zero-velocity surface. It is interesting to compare the above limiting situation with that of the standard Taylor–Couette flow. In the standard configuration, the core of the flow has a constant mean angular momentum at sufficiently high Reynolds numbers (Smith & Townsend 1982; Lewis & Swinney 1999; Dong 2007); therefore, the mean azimuthal velocity approaches a function $\sim 1/r$ in the core at sufficiently high Reynolds numbers.

The mean azimuthal velocity profiles (figure 15a) demonstrate regions of high-velocity-gradient values near both walls and a region of low-velocity gradient in the middle of the gap, exhibiting a boundary-layer-like feature. We can define a length scale to characterize the thickness of the near-wall high-velocity-gradient regions, which can be regarded as an 'effective boundary-layer thickness'. Note that this length scale differs from the boundary-layer thickness in the usual sense, i.e. in the presence of an inviscid flow core or inviscid free stream (such as in flat-plate turbulent boundary layers) (Panton 2005). Since the Taylor–Couette system is confined, the boundary layers originating from both walls together fill the entire gap with viscous flow. We can define the thickness of these near-wall regions of high-velocity gradients based on the distribution of the quantity $J_\nu^\omega = -r^3\nu(\partial\langle\omega\rangle/\partial r)$, which is a component of the angular velocity current J^ω (see (4.1)). Figure 13 indicates that J_ν^ω has the same value as J^ω at both cylinder walls and has a low and approximately constant value in the middle portion of the gap corresponding to low-velocity-gradient values. We will define the boundaries of the high-velocity-gradient layers as radial locations, r_δ, corresponding to $J_\nu^\omega(r_\delta) = J_\nu^\omega|_{min} + (J^\omega - J_\nu^\omega|_{min}) \times 10\,\%$, where $J_\nu^\omega|_{min}$ is the minimum value of J_ν^ω within the cylinder gap. We find that the 10 % fraction in the definition, although somewhat arbitrary, has provided a reasonable measure for the thickness at all the Reynolds numbers considered here. We have computed the effective boundary-layer thickness (i.e. distance of r_δ to cylinder walls), and in figure 16 we plot it as a function of the inner-/outer-cylinder Reynolds number. First of all, we observe the asymmetry between the high-velocity-gradient layers of the two walls, with the thickness at the outer cylinder two to three times as large as that at the inner one. As the Reynolds number increases, the thickness decreases for both walls. For Reynolds numbers $Re_i = -Re_o \geqslant 1500$, it appears to scale as a function $\sim Re_i^\xi$ (straight line in the plot), $\xi = -0.730$ for the inner cylinder and $\xi = -0.504$ for the outer cylinder; there is a deviation from this scaling if the data point at $Re_i = -Re_o = 500$ is included. In several theoretical analyses (see e.g. Eckhardt, Grossman & Lohse 2000; Grossmann & Lohse (2000); van den Berg *et al.* 2003) of Taylor–Couette flows, a Blasius-type laminar boundary layer was assumed (and the two layers at the walls were assumed to be symmetric), which led to a scaling relation with $\xi = -0.5$. Barcilon & Brindley (1984) assumed a linear velocity profile within the boundary layer.

In figure 17, we compare profiles of the r.m.s. azimuthal fluctuation velocity, u'_θ, normalized by the rotation velocity of the inner wall U_i. The profiles exhibit a

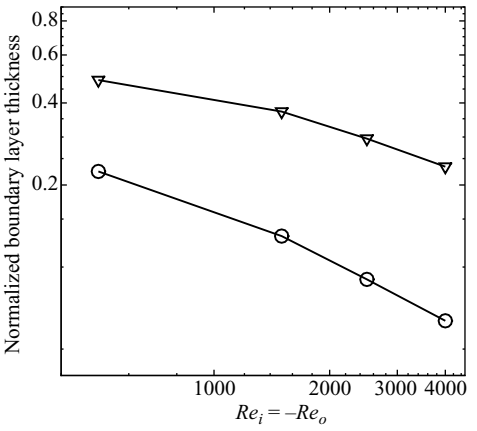

FIGURE 16. Effective boundary-layer thickness at cylinder walls (normalized by the gap width) versus Reynolds number. ○, inner walls; ▽, outer walls.

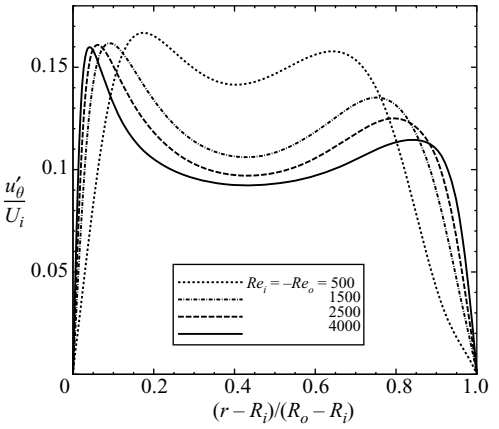

FIGURE 17. Comparison of profiles of r.m.s. azimuthal fluctuation velocity u'_θ at different Reynolds numbers.

double-peak feature typical of wall-bounded turbulent flows. At $Re_i = -Re_o = 500$, high fluctuations are observed in the middle region of the gap, slightly shifted toward the inner cylinder, while fluctuations in regions near both walls are relatively weak. This indicates that Taylor vortices are predominantly active in the middle region (toward the inner cylinder) of the gap (figure 5*a*) at this Reynolds number. As the Reynolds number increases, the two peaks in the profiles move toward the cylinder walls, and the fluctuations in the core of the flow become weaker compared to the near-wall regions. Near the inner cylinder, the r.m.s. velocity profile is characterized by a sharp narrow peak, with the strongest fluctuation intensity; near the outer cylinder, however, the peak is wide with a markedly lower fluctuation intensity.

Figure 18 compares profiles of the normalized Reynolds stress $\langle u'_r u'_\theta \rangle / U_i^2$ at different Reynolds numbers. Note that both the Taylor vortices (at low Reynolds numbers) and the small-scale azimuthal vortices (with increasing Reynolds number) tend to promote a positive correlation between the radial and azimuthal fluctuation velocities. For example, a positive fluctuation radial velocity tends to transport fluids of higher azimuthal velocities (respectively, of less negative azimuthal velocities) away from

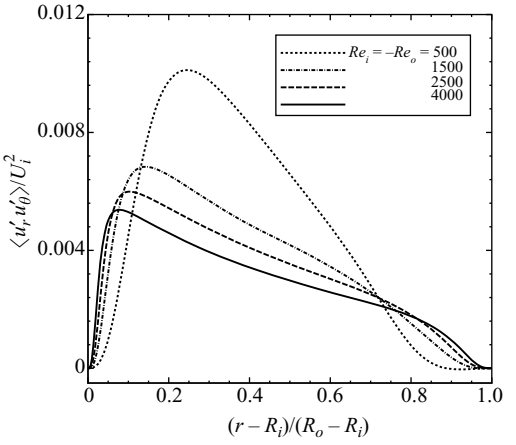

FIGURE 18. Comparison of profiles of Reynolds stress $\langle u_r' u_\theta' \rangle / U_i^2$ at different Reynolds numbers.

the inner wall (respectively, toward the outer wall); a negative fluctuation radial velocity tends to transport fluids of lower azimuthal velocities (respectively, with more negative azimuthal velocities) toward the inner wall (respectively, away from the outer wall). Therefore, we generally observe a positive Reynolds stress $\langle u_r' u_\theta' \rangle$ in the cylinder gap (figure 18). The distribution exhibits a single prominent peak toward the inner cylinder, which is different from turbulent channels where two near-wall peaks can be observed. At $Re_i = -Re_o = 500$, high Reynolds-stress values are observed in the middle region (shifted toward inner cylinder), as expected from the vortex distributions of the instantaneous flow (figure 5*a*). The profile exhibits a relatively long tail with essentially zero Reynolds stress near the outer cylinder, for the Taylor vortices are confined to the middle and inner portions of the gap as evidenced from the instantaneous flow patterns (figure 5*a*). As the Reynolds number increases, the locations of the peak Reynolds stress moves toward the inner cylinder, and the tail of zero Reynolds stress in the profiles shrinks notably; furthermore, the slope of the profiles increases in magnitude in a region near the outer cylinder, which appears to suggest a trend that another peak may emerge near the outer cylinder as the Reynolds number further increases. Note that at high Reynolds numbers, the Reynolds-stress profile scales essentially as a function $\sim 1/r^2$ in the core of the gap (with a shift toward the inner cylinder). This can be inferred from (4.1) by noting the constant angular velocity current and that the derivative of the angular velocity essentially vanishes in the core of flow (see figure 13).

5. Comparison between standard and counter-rotating Taylor–Couette turbulence – effect of the Coriolis force

Turbulent Taylor–Couette flows in a standard configuration and in a counter-rotating configuration share some common characteristics. For example, as the Reynolds number increases, both flows are dominated by azimuthal vortices with scales much smaller than the cylinder gap, whereas Taylor vortices cease to exist in the instantaneous sense. At high Reynolds numbers, Taylor vortices exist only in the mean sense as manifested by the time-averaged flow field. Near-wall streaks form

herringbone-like patterns not only in the standard Taylor-Couette configuration, but also in the counter-rotating configuration (figure 7).

Despite these commonalities, there are notable differences between the two configurations. First, based on the Rayleigh criterion, the flow is linearly unstable everywhere in the standard configuration, whereas in the counter-rotating configuration, it is linearly stable in the outer portion of the gap (beyond the zero azimuthal velocity surface) and unstable only in the inner portion. This appears to have a great effect on the distributions of Taylor vortices. In the standard configuration, Taylor vortices are observed to occupy the entire gap, in the instantaneous sense at low Reynolds numbers and in the time-averaged sense as the Reynolds number increases (Dong 2007). In contrast, in the counter-rotating configuration, Taylor vortices are confined to the inner portion of the gap, and there exists a layer of fluid near the outer cylinder that the Taylor vortex motions are unable to penetrate in the time-averaged sense (figure 14). Secondly, compared to those in the standard configuration, herringbone streaks in the counter-rotating configuration tend to be less populous and more coherent and have notably lower tilting angles (Dong 2008). Thirdly, in the standard configuration, the core of the flow has an essentially constant angular momentum $0.5R_iU_i$ (Smith & Townsend 1982; Lewis & Swinney 1999; Dong 2007); In contrast, in the counter-rotating configuration, although both its value and the slope of its profile are low in the core of the flow, the angular momentum decreases monotonically with respect to the radial coordinate.

In order to provide a sense of quantitative differences between the standard and counter-rotating Taylor–Couette turbulence, we transform the counter-rotating configuration into the standard configuration by using a rotating frame of reference. We compare these two configurations and demonstrate the effects of the Coriolis force on the mean and fluctuation velocities. Consider a frame of reference rotating at an angular velocity $\boldsymbol{\Omega}$, $\boldsymbol{\Omega} = \Omega_o \boldsymbol{e}_z$ (where Ω_o is the angular velocity of the outer cylinder and $\boldsymbol{e}_z$ is the unit vector in the z-direction), around the z-axis of the fixed frame of reference. In this rotating reference frame, the Navier–Stokes equation can be expressed as (Tritton 1988; Dubrulle *et al.* 2005)

$$\frac{\partial \boldsymbol{u}}{\partial t} + \boldsymbol{u}\cdot\nabla\boldsymbol{u} = -\frac{1}{\rho}\nabla\Pi - 2\boldsymbol{\Omega}\times\boldsymbol{u} + \nu\nabla^2\boldsymbol{u}, \tag{5.1}$$

where t is time, and ρ is the density of the fluid. In (5.1), $\boldsymbol{u}$ is the velocity in the rotating frame of reference and is related to the velocity in the fixed reference frame, $\boldsymbol{u}^F$, by $\boldsymbol{u} = \boldsymbol{u}^F - \boldsymbol{\Omega}\times\boldsymbol{r}$, where $\boldsymbol{r}$ is the position vector. The generalized pressure Π, $\Pi = p - \rho|\boldsymbol{\Omega}|^2 r'^2/2$ (where p is the pressure and r' is the distance to the axis of rotation, $r' = |\boldsymbol{r} - ((\boldsymbol{r}\cdot\boldsymbol{\Omega})\boldsymbol{\Omega}/\boldsymbol{\Omega}\cdot\boldsymbol{\Omega}|)$, has included the effect of the centrifugal force, $-\boldsymbol{\Omega}\times(\boldsymbol{\Omega}\times\boldsymbol{r})$. The term $-2\boldsymbol{\Omega}\times\boldsymbol{u}$ represents the Coriolis force.

In this rotating frame of reference, the outer cylinder becomes stationary, and the inner cylinder rotates at an angular velocity $(\Omega_i - \Omega_o)$. For the cases considered here, $Re_i = -Re_o$, the inner wall rotates at a velocity $(\Omega_i - \Omega_o)R_i = (1+\eta)\Omega_i R_i$ in the rotating frame of reference. Comparison between the counter-rotating configuration at $Re_i = -Re_o$ in the rotating frame of reference and the standard configuration in the fixed frame of reference at Reynolds number $(1+\eta)Re_i$ suggests that the only difference between them is the Coriolis force in (5.1). Of course, the pressure will also be different owing to the centrifugal force. The two flows are dynamically similar except for the Coriolis force.

In the following, we compare the counter-rotating flow of $Re_i = -Re_o = 4000$ (in the rotating reference frame) and the standard Taylor–Couette flow at Reynolds

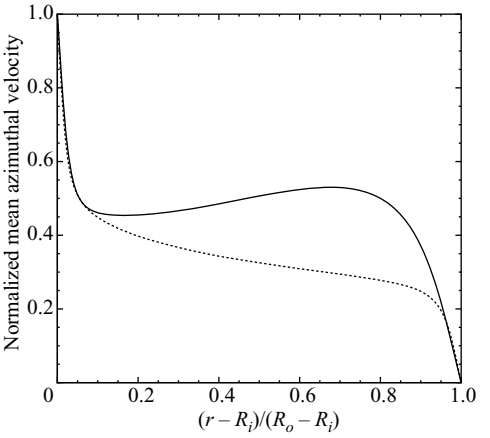

FIGURE 19. Comparison of mean azimuthal velocity profiles between —, CRTC flow at $Re_i = -Re_o = 4000$ (in a frame rotating with the outer cylinder) and . . ., the TC flow at $Re = 6000$ (fixed frame of reference). The velocity has been normalized by the inner cylinder rotation velocity in their respective reference frames.

number $Re = 6000$ (in the fixed reference frame) to demonstrate the effects of the Coriolis force on the flow characteristics. In figure 19, we compare the mean azimuthal velocity profiles (averaged in time and in the axial and azimuthal directions) of the two flows, which have been normalized by the inner-cylinder rotation velocities in their respective frames of reference. The mean Coriolis force, averaged over time and also along the axial and azimuthal directions, is in the negative radial direction; its azimuthal component is essentially zero. The presence of the Coriolis force in the rotating frame of reference has only marginally affected the mean flow in the near-wall regions (slightly reducing the magnitudes of the velocity gradient at the walls). However, it has dramatically modified the mean velocity profile in the core; the mean azimuthal velocity has been substantially increased, especially toward the outer cylinder, resulting in a positive velocity gradient in the middle region of the gap.

In figure 20, we compare profiles of the second-order statistical quantities between the counter-rotating configuration ($Re_i = -Re_o = 4000$) in the rotating reference frame and the standard configuration ($Re = 6000$) in the fixed reference frame. Figure 20(a) is a comparison of the r.m.s. azimuthal fluctuation velocity (u'_θ), normalized by the inner wall rotating velocity in the respective frames of reference. Both configurations result in profiles with similar shapes. However, some prominent differences can be noted. In the standard configuration, the profile is characterized by two distinct sharp peaks near the walls; in contrast, the distribution in the counter-rotating configuration exhibits a blunt wide peak near the outer cylinder, whereas the peak near the inner cylinder is sharp. Compared to the counter-rotating system, peak velocity fluctuations in the standard configuration occur at locations closer to both cylinder walls. The presence of the Coriolis force, which substantially increases the mean azimuthal velocity in the bulk of the flow, has also notably enhanced the azimuthal r.m.s. velocity fluctuations, except in regions very close to the walls. Figure 20(b) shows a comparison of profiles of the Reynolds stress $\langle u'_r u'_\theta \rangle$, normalized by the inner wall velocity squared in the respective frames of reference of the two configurations. The profiles of the two configurations have similar shapes and exhibit some common

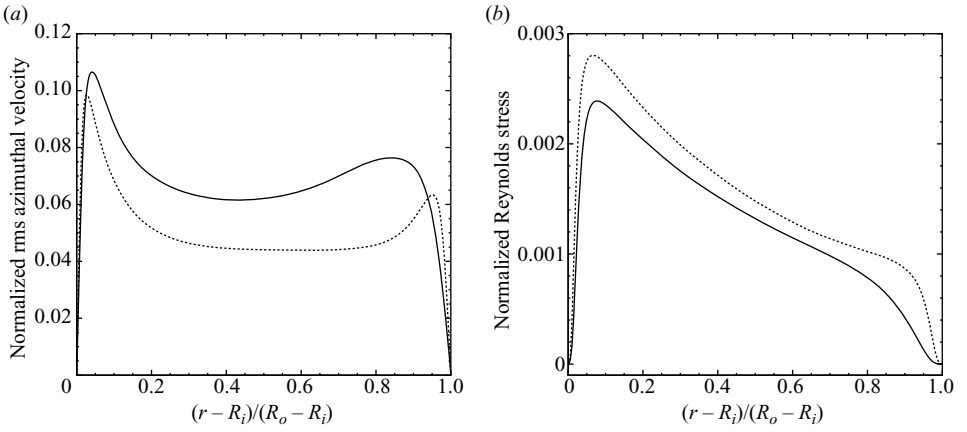

FIGURE 20. Comparison of statistics between —, CRTC flow at $Re_i = -Re_o = 4000$ (rotating frame of reference) and ..., TC flow at $Re = 6000$ (fixed frame of reference): (*a*) r.m.s. azimuthal velocity u'_θ/U_0, and (*b*) Reynolds stress $\langle u'_r u'_\theta \rangle / U_0^2$. U_0 is the inner wall rotation velocity in their respective reference frames.

characteristics. However, the values are notably larger in the standard configuration than in the counter-rotating one, indicating a decrease in the correlation between the azimuthal and axial fluctuation velocities owing to the Coriolis force. We can also note a longer tail with essentially zero Reynolds stress near the outer cylinder in the profile of the counter-rotating configuration.

6. Concluding remarks

We have investigated the dynamical and statistical features of the turbulent flow between counter-rotating concentric cylinders employing detailed three-dimensional direct numerical simulations. The study is for a radius ratio $\eta = 0.5$ at inner-/outer-cylinder Reynolds numbers ranging from 500 to 4000 while the condition $Re_i = -Re_o$ is maintained.

As the Reynolds number increases, the prevailing structures in Taylor–Couette turbulence are the azimuthal vortices with scales much smaller than the cylinder gap. This is true for both the counter-rotating system studied here and the standard configuration in previous work (Dong 2007). Taylor vortices (with scales commensurate with the cylinder gap) can be observed instantaneously only at low Reynolds numbers. At high Reynolds numbers, they cease to exist in the instantaneous sense, and can be observed only in the time-averaged sense. The collective effect of the instantaneous small-scale vortices manifests as organized Taylor vortex motions in the cylinder gap.

For the shear flow over a curvature, Rayleigh (1916) shows that the flow is subject to an inviscid centrifugal instability if the magnitude of the angular momentum decreases along the radius of curvature anywhere in the flow (necessary and sufficient condition). This is referred to as the Rayleigh criterion. When applied to the circular Couette flow between counter-rotating cylinders, this means that the inner portion of the flow (inside the zero-velocity surface) suffers from an inviscid instability while the outer portion of the flow is stable. In the presence of viscosity the Rayleigh criterion is not directly applicable (Saric 1994; Esser & Grossman 1996). Results from the present

study nonetheless show that it has a profound effect on the dynamics and statistics of the counter-rotating Taylor–Couette turbulence. For example, at high Reynolds numbers, although the instantaneous small-scale azimuthal vortices dominate the entire cylinder gap, the Taylor vortex motions manifested from the time-averaged mean field, are unable to penetrate a thin layer of fluid near the outer cylinder wall. The effect is also manifested in the blunt wide peak near the outer cylinder in the r.m.s. fluctuation velocity profiles.

The presence of streaks in near-wall regions is a signature of wall-bounded turbulence. Near-wall streaks have been observed in several types of flow, e.g. turbulent channels, flat-plate boundary layers, and plane Couette flows (Kline *et al.* 1967; Smith & Metzler 1983). The unique effect in Taylor–Couette turbulence is that the near-wall streaks form intricate herringbone-like patterns. Herringbone streaks were first observed by Barcilon *et al.* (1979) in a visualization study for a standard Taylor–Couette system. These structures have been reproduced by numerical simulations and investigated in detail (Dong 2007, 2008). Results of the present study, together with the evidence from previous investigations, suggest that herringbone streaks appear to be an intrinsic feature of turbulent Taylor–Couette systems. We are confident that this is true for the standard and counter-rotating configurations, based on the present and previous studies; however, it is still unknown for the co-rotating configuration (both cylinders rotating in the same direction).

By using a rotating frame of reference, the counter-rotating configuration of the Taylor–Couette system can be transformed into the standard configuration, and vice versa. In terms of Navier–Stokes equations, the main difference between them would be the additional Coriolis force in the rotating frame of reference. Comparison between the counter-rotating flow in a rotating reference frame and standard flow in the fixed reference frame has revealed the effects of the Coriolis force on the flow characteristics. The Coriolis force has significantly modified the distributions of statistical quantities such as the mean flow, the r.m.s. velocity fluctuation, and the Reynolds stress.

It is also interesting to compare features of the counter-rotating turbulent Taylor–Couette flow studied here with those of the turbulent plane Couette flow (see e.g. Bech *et al.* 1995). The most prominent difference is the asymmetry of flow quantities, both instantaneous and statistical, between the two walls in the counter-rotating Taylor–Couette situation, unlike in the plane Couette flow. These include the near-wall velocity spectra (figure 9), profiles of the mean velocity (figure 15*a*), r.m.s. fluctuation velocity (figure 17), and the Reynolds stress (figure 18). In Taylor–Couette flow, the region near the inner cylinder accommodates notably stronger turbulent fluctuations, a larger mean velocity gradient, and much higher Reynolds-stress values than that near the outer cylinder. In contrast, in plane Couette turbulence, the physical quantities (such as profiles of the mean velocity, r.m.s. fluctuation velocity and the Reynolds stress) are symmetric (or anti-symmetric) at the two walls (Bech *et al.* 1995). This symmetry in plane Couette turbulence persists even in the presence of strong system rotation (Bech & Andersson 1997). The difference between the two flows is a manifestation of the curvature effect of the Taylor–Couette geometry, which has a smaller radius of curvature at the inner cylinder than at the outer one.

The author gratefully acknowledges the support from NSF and DOE. Computer time was provided by the TeraGrid through an MRAC grant and by the Rosen Center for Advanced Computing (RCAC) at Purdue University.

REFERENCES

Adrian, R. J. 2007 Hairpin vortex organization in wall turbulence. *Phys. Fluids* **19**, 041301.

Andereck, C. D., Liu, S. S. & Swinney, H. L. 1986 Flow regimes in a circular Couette system with independently rotating cylinders. *J. Fluid Mech.* **164**, 155–183.

antonijoan, J., Marques, F. & Sanchez, J. 1998 Non-linear spirals in the Taylor–Couette problem. *Phys. Fluids* **10**, 829–838.

Barcilon, A. & Brindley, J. 1984 Organized structures in turbulent Taylor–Couette flow. *J. Fluid Mech.* **143**, 429–449.

Barcilon, A., Brindley, J., Lessen, M. & Mobbs, F. R. 1979 Marginal instability in Taylor–Couette flows at a high Taylor number. *J. Fluid Mech.* **94**, 453–463.

Bech, K. H. & Andersson, H. I. 1997 Turbulent plane Couette flow subject to strong system rotation. *J. Fluid Mech.* **347**, 289–314.

Bech, K. H., Tillmark, N., Henrikalfredsson, P. & Andersson, H. I. 1995 An investigation of turbulent plane Couette flow at low Reynolds numbers. *J. Fluid Mech.* **286**, 291–325.

van den Berg, T. H., Doering, C. R., Lohse, D. & Lathrop, D. P. 2003 Smooth and rough boundaries in turbulent Taylor–Couette flow. *Phys. Rev.* E **68**, 036307.

Bilgen, E. & Boulos, E. 1973 Functional dependence of torque coefficient of coaxial cylinders gap width and Reynolds numbers. *Trans. ASME* I: *J. Fluids Engng* **95**, 122–126.

Coles, D. 1965 Transition in circular Couette flow. *J. Fluid Mech.* **21**, 385–425.

Colovas, P. W. & Andereck, C. D. 1997 Turbulent bursting and spatiotemporal intermittency in the counterrotating Taylor–Couette system. *Phys. Rev.* E **55**, 2736–2741.

Coughlin, K. & Marcus, P. S. 1996 Turbulent bursts in Couette–Taylor flow. *Phys. Rev. Lett.* **77**, 2214–2217.

Dong, S. 2007 Direct numerical simulation of turbulent Taylor–Couette flow. *J. Fluid Mech.* **587**, 373–393.

Dong, S. 2008 Herringbone streaks in Taylor–Couette turbulence. *Phys. Rev.* E **77**, 035301.

Dong, S. & Karniadakis, G. E. 2004 Dual-level parallelism for high-order CFD methods. *Parallel Comput.* **30**, 1–20.

Dong, S. & Karniadakis, G. E. 2005 DNS of flow past a stationary and oscillating cylinder at $Re = 10\,000$. *J. Fluids Struct.* **20**, 519–531.

Dong, S., Karniadakis, G. E., Ekmekci, A. & Rockwell, D. 2006 A combined direct numerical simulation–particle image velocimetry study of the turbulent near wake. *J. Fluid Mech.* **569**, 185–207.

Dong, S., Triantafyllou, G. S. & Karniadakis, G. E. 2008 Elimination of vortex streets in bluff-body flows. *Phys. Rev. Lett.* **100**, 204501.

Dubrulle, B., Dauchot, O., Daviaud, F., Longaretti, P.-Y., Richard, D. & Zahn, J.-P. 2005 Stability and turbulent transport in Taylor–Couette flow from analysis of experimental data. *Phys. Fluids* **17**, 095103.

Eckhardt, B., Grossman, S. & Lohse, D. 2000 Scaling of global momentum transport in Taylor–Couette and pipe flow. *Eur. Phys. J.* B **18**, 541–544.

Eckhardt, B., Grossmann, S. & Lohse, D. 2007 Torque scaling in turbulent Taylor–Couette flow between independently rotating cylinders. *J. Fluid Mech.* **581**, 221–250.

Esser, A. & Grossman, S. 1996 Analytic expression for Taylor–Couette stability boundary. *Phys. Fluids* **8**, 1814–1819.

Goharzadeh, A. & Mutabazi, I. 2001 Experimental characterization of intermittency regimes in the Couette–Taylor system. *Eur. Phys. J.* B **19**, 157–162.

Grossmann, S. & Lohse, D. 2000 Scaling in thermal convection: a unifying theory. *J. Fluid Mech.* **407**, 27–56.

Hegseth, J. J., Andereck, C. D., Hayot, F. & Pomeau, Y. 1989 Spiral turbulence and phase dynamics. *Phy. Rev. Lett.* **62**, 257–260.

Hoffmann, C., Lucke, M. & Pinter, A. 2004 Spiral vortices and Taylor vortices in the annulus between rotating cylinders and the effect of an axial flow. *Phys. Rev.* E **69**, 056309.

Hoffmann, C., Lucke, M. & Pinter, A. 2005 Spiral vortices traveling between two rotating defects in Taylor–Couette system. *Phys. Rev.* E **72**, 056311.

Hristova, H., Roch, S., Schmid, P. J. & Tuckerman, L. S. 2002 Transient growth in Taylor–Couette flow. *Phys. Fluids* **14**, 3475–3484.

Jeong, J. & Hussain, F. 1995 On the identification of a vortex. *J. Fluid Mech.* **285**, 69–94.

Karniadakis, G. E. & Sherwin, S. J. 2005 *Spectral/hp Element Methods for Computational Fluid Dynamics*, 2nd edn. Oxford University Press.

Karniadakis, G. E., Israeli, M. & Orszag, S. A. 1991 High-order splitting methods for the incompressible Navier–Stokes equations. *J. Comput. Phys.* **97**, 414–443.

Kline, S. J., Reynolds, W. C., Schraub, F. A. & Runstadler, P. W. 1967 The structure of turbulent boundary layers. *J. Fluid Mech.* **30**, 741–773.

Lewis, G. S. & Swinney, H. L. 1999 Velocity structure functions, scaling, and transitions in high-Reynolds-number Couette–Taylor flow. *Phys. Rev.* E **59**, 5457–5467.

Litschke, H. & Roesner, K. G. 1998 New experimental methods for turbulent spots and turbulent spirals in the Taylor–Couette flow. *Exps. Fluids* **24**, 201–209.

Panton, R. L. 2005 *Incompressible Flow*. John Wiley.

Pope, S. B. 2000 *Turbulent Flows*. Cambridge University Press.

Prigent, A., Gregoire, G., Chate, H., Dauchot, O. & van Saarloos, W. 2002 Large-scale finite-wavelength modulation within turbulent shear flows. *Phys. Rev. Lett.* **89**, 014501.

Racina, A. & Kind, M. 2006 Specific power and local micromixing times in turbulenct Taylor–Couette flow. *Exps. Fluids* **41**, 513–522.

Rayleigh, Lord 1916 On the dynamics of revolving fluids. *Scientific Papers*, vol. **6**, pp. 447–453.

Robinson, S. K. 1991 Coherent motions in the turbulent boundary layer. *Annu. Rev. Fluid Mech.* **23**, 601.

Saric, W. S. 1994 Görtler vortices. *Annu. Rev. Fluid Mech.* **26**, 379–409.

Smith, C. R. & Metzler, S. P. 1983 The characteristics of low-speed streaks in the near-wall region of a turbulent boundary layer. *J. Fluid Mech.* **129**, 27–54.

Smith, G. P. & Townsend, A. A. 1982 Turbulent Couette flow between concentric cylinders at large Taylor numbers. *J. Fluid Mech.* **123**, 187–217.

Tritton, D. J. 1988 *Physical Fluid Dynamics*. Oxford University Press.

Vaezi, V., Oh, E. S. & Aldredge, R. C. 1997 High-intensity turbulence measurements in a Taylor–Couette flow reactor. *Expl Thermal Fluid Sci.* **15**, 424–431.

Van Atta, C. 1966 Exploratory measurements in spiral turbulence. *J. Fluid Mech.* **25**, 495–512.

Wei, T., Kline, E. M., Lee, S. H. K. & Woodruff, S. 1992 Görtler vortex formation at the inner cylinder in Taylor–Couette flow. *J. Fluid Mech.* **245**, 47–68.

Wendt, F. 1933 Turbulente stromungen zwischen zwei eorierenden konaxialen zylindem. *Ing. Arch.* **4**, 577–595.